

THESIS

**A Study of Baseline Compensation  
System for Stable Operation of  
Gravitational-wave Telescope**

**Koseki Miyo**

*Department of Physics  
University of Tokyo*

MMM 2020



# Contents

<b>1</b>	<b>Background</b>	<b>7</b>
1.1	Gravitational-wave . . . . .	7
1.1.1	... . . . .	7
1.2	Sources of Gravitational-wave . . . . .	7
1.2.1	... . . . .	7
1.3	Interferometric Gravitational-wave detection . . . . .	7
1.3.1	Detection Principle . . . . .	7
1.3.2	Michelson Interferometer . . . . .	8
1.3.3	Null Measurement . . . . .	9
1.4	Summary of the Chapter . . . . .	9
<b>2</b>	<b>KAGRA</b>	<b>11</b>
2.1	Overview . . . . .	11
2.1.1	... . . . .	11
2.1.2	... . . . .	11
2.2	KAGRA Tunnel . . . . .	11
2.2.1	Tunnel Design . . . . .	11
2.2.2	Geological features . . . . .	11
2.3	Main Interferometer . . . . .	11
2.3.1	Overview . . . . .	11
2.3.2	Main Interferometer . . . . .	12
2.4	Vibration Isolation System . . . . .	12
2.4.1	Overview . . . . .	12
2.4.2	Type-A Suspension System . . . . .	12
2.5	Summary of the Chapter . . . . .	12
<b>3</b>	<b>Seismic Noise</b>	<b>13</b>
3.1	Theory of seismic waves . . . . .	13
3.1.1	Seismic Waves in Isotropic and Homogeneous Medium . . . . .	13
3.1.2	Reduction Effect in the Deep Sites . . . . .	15
3.1.3	Reduction Effect of the Short Baseline . . . . .	15
3.2	Seismic Noise . . . . .	17

3.2.1	Cultural Noises . . . . .	17
3.2.2	Natural Noises . . . . .	18
3.2.3	Spatial Seismic Noise Changes . . . . .	20
3.3	Study of Temporal Seismic Noise at KAGRA . . . . .	20
3.3.1	Overview . . . . .	20
3.3.2	Experimental Arrangement . . . . .	21
3.3.3	Data Selection . . . . .	22
3.3.4	Data Processing . . . . .	22
3.3.5	Results . . . . .	22
3.4	Study of Differential Motion Reduction . . . . .	23
3.4.1	Introduction . . . . .	23
3.4.2	Overview . . . . .	23
3.4.3	Reduction in X-arm Scale . . . . .	25
3.4.4	Reduction in Other Short Scale . . . . .	25
3.5	Summary of the Chapter . . . . .	25
<b>4</b>	<b>Geophysics Interferometer (GIF)</b>	<b>27</b>
4.1	Overview . . . . .	27
4.1.1	Laser Strainmeter for Geophysics . . . . .	27
4.1.2	Motivation in GW detectors . . . . .	27
4.2	Working Principle . . . . .	27
4.2.1	Asymmetric Michelson Interferometer . . . . .	27
4.2.2	Response to the seismic strain . . . . .	27
4.2.3	Signal Detection Scheme . . . . .	28
4.2.4	Noise . . . . .	28
4.3	Optics Design . . . . .	29
4.3.1	Overview . . . . .	29
4.3.2	Design Concept . . . . .	29
4.3.3	Input Output Optics . . . . .	30
4.3.4	Core Optics . . . . .	30
4.3.5	Frequency Stabilized Laser . . . . .	30
4.4	Data Acquisition System . . . . .	30
4.4.1	Realtime Processing . . . . .	30
4.4.2	... . . . .	30
4.5	Summary of the Chapter . . . . .	30
<b>5</b>	<b>Arm Length Compensation System for Global Seismic Control</b>	<b>31</b>
5.1	Introduction . . . . .	31
5.2	Basics in Vibration Isolation and Control Technique . . . . .	33
5.2.1	Passive Vibration Isolation . . . . .	33
5.2.2	Active Vibration Isolation . . . . .	33
5.2.3	Sensor Based Control Technique . . . . .	33

5.2.4	2 Types Feedforward Control Techniques . . . . .	33
5.2.5	Toward the Global Seismic Control . . . . .	33
5.3	Difficulties in the Global Seismic Control . . . . .	33
5.3.1	Overview . . . . .	33
5.3.2	Actuator Range Limit . . . . .	33
5.3.3	... . . . .	33
5.3.4	... . . . .	33
5.4	Arm Length Compensation Using Geophysics Interferometer . . . . .	33
5.4.1	Concept . . . . .	33
5.4.2	Geophysics Interferometer for Sensing the Arm Length . . . . .	33
5.4.3	Arm Length Compensation . . . . .	33
5.4.4	Requirements . . . . .	33
5.5	Summary of the Chapter . . . . .	33
<b>6</b>	<b>Demonstration of Arm Length Compensation Control</b>	<b>35</b>
6.1	Experimental Arrangement . . . . .	35
6.1.1	... . . . .	35
6.2	Results . . . . .	35
6.2.1	... . . . .	35
6.3	Discussion and Summary of the Chapter . . . . .	35
6.3.1	Discussion . . . . .	35
6.3.2	Summary . . . . .	35
<b>7</b>	<b>Conculusion and Future Directions</b>	<b>37</b>
7.1	Conclusion . . . . .	37
7.2	Future Directions . . . . .	37
<b>A</b>	<b>Theory of Seismic Waves</b>	<b>39</b>
A.1	Rayleigh 波 . . . . .	39
A.2	Depth Dependence . . . . .	39



# Chapter 1

## Background

### 1.1 Gravitational-wave

#### 1.1.1 ...

### 1.2 Sources of Gravitational-wave

#### 1.2.1 ...

### 1.3 Interferometric Gravitational-wave detection

#### 1.3.1 Detection Principle

地上の大型重力波検出器の基本要素は Michelson 型レーザー干渉計である。プラスモードの重力波が Fig.4.4 に示すような Michelson 型レーザー干渉計を垂直に通過する場合を考える。

### 1.3.2 Michelson Interferometer

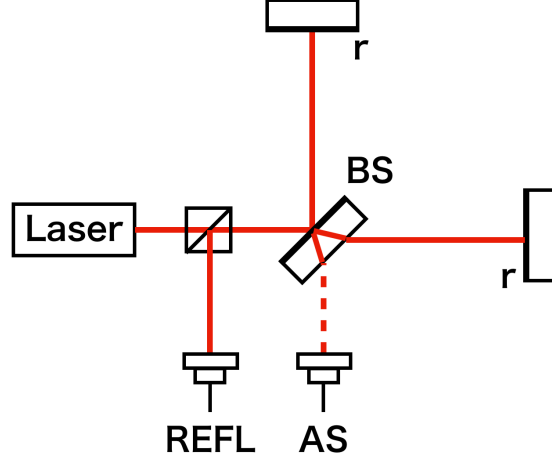


**Figure 1.1:** Michelson Interferometer.

Michelson interferometer is a converter from the optical phase difference of two lights to the amplitude modulation of a single light. Consider about the interferometer shown in Fig. 1.1. Incident light can be written as,

$$E_{\text{in}} = E_0 e^{i\omega t}, \quad (1.1)$$

where  $E_0$  is the amplitude and  $\omega_0$  is the angular frequency of the laser field. Two lights split by the Beam Splitter (BS) interfere at the Anti-symmetric (AS) port and Reflection (REFL) port. The output field at the AS port is represented as,

$$E_{\text{AS}} = -\frac{1}{2}rE_0 e^{i(\omega_0 t - \phi_x)} + \frac{1}{2}rE_0 e^{i(\omega_0 t - \phi_y)}, \quad (1.2)$$

where  $r$  denotes the amplitude reflectivity of the end mirrors, and  $\phi_x$  and  $\phi_y$  are the phase delays due to the light traveling in the  $x$  and  $y$  arms. This output signal can be represented as a single field as,

$$E_{\text{AS}} = irE_0 e^{i(\omega_0 t - (\phi_x + \phi_y)/2)} \sin\left(\frac{\phi_x - \phi_y}{2}\right). \quad (1.3)$$

We find that the amplitude of the output light is a function of the difference between two phases;  $\phi_x - \phi_y$ . Furthermore, the power of output light at the AS port is obtained by squaring the Eq. 1.3,

$$P_{\text{AS}} = (rE_0)^2 [1 - \cos(\phi_x - \phi_y)] \quad (1.4)$$



Similarly, power of the output light as REFL port is written as,

$$P_{\text{REFL}} = (rE_0)^2 [1 + \cos(\phi_x - \phi_y)]. \quad (1.5)$$

Therefore, we can measure the optical phase difference as the amplitude changes using a Photo Detector (PD) and detect GWs.

### 1.3.3 Null Measurement

#### Shot Noise

Shot noise is the optical readout noise associated with the discrete nature of photons and electric charges. 光のパワーは

#### Control Noise

## 1.4 Summary of the Chapter



## Chapter 2

# KAGRA

### 2.1 Overview

#### 2.1.1 ...

#### 2.1.2 ...

### 2.2 KAGRA Tunnel

#### 2.2.1 Tunnel Design

KAGRA tunnel is excavated in the Kamioka mine in Hida, Gifu, Japan [1]. The tunnel is consisted of two floors. 干渉計を構成するほとんどの鏡は 1 階に設置された防振装置で懸架されているが、腕共振器を構成する 4 つの鏡は 1 階から 14m の高さにある 2 階から懸架されている。

The tunnel is locate under 200 m from ground surface to decrease the seismic noise effectively.

#### 2.2.2 Geological features

Hida region to which Kamioka belongs is a ancient region in Japan island [2].

The main bedrock is the geniss.

### 2.3 Main Interferometer

#### 2.3.1 Overview

KAGRA is a cryogenic intergerometric gravitational-wave detector constructed at the underground site of Kamioka mine [3].

### 2.3.2 Main Interferometer

#### Design

The design of KAGRA interferometer is dual recycled Fabry-Perot Michelson interferometer [4][5].

## 2.4 Vibration Isolation System

### 2.4.1 Overview

KAGRA has 4 types vibration isolation system.

### 2.4.2 Type-A Suspension System

Type-A suspensions are developed [6].

## 2.5 Summary of the Chapter

## Chapter 3

# Seismic Noise

Seismic noise limits the low-frequency sensitivity of gravitational-wave detectors and degrades the duty cycle of that. In this chapter, 以下の事柄を述べる;

- 地面振動の数学的な理解とその性質 (§3.1)
- 一般的な地面振動のノイズ源 (§3.2)
- KAGRA の地面振動の時間的な特徴 (§3.3)
- KAGRA の地面振動の空間的な特徴 (§3.4)

### 3.1 Theory of seismic waves

Here we introduce characteristics of the seismic wave that will be useful in our later understanding and modeling of seismic effects.

#### 3.1.1 Seismic Waves in Isotropic and Homogeneous Medium

The elastodynamic wave equation is given by

$$\rho \ddot{\mathbf{u}} = (\lambda + 2\mu) \nabla(\nabla \cdot \mathbf{u}) - \mu \nabla \times (\nabla \times \mathbf{u}), \quad (3.1)$$

where  $\mathbf{u}$  is the displacement field vector of the medium,  $\rho$  denotes density of the medium, and  $\lambda, \mu$  are Lamé's first and second constant.

##### Body Waves

From 3.1, we can obtain two characteristic waves; primary wave (P-wave) which is a longitudinal wave and secondary wave (S-wave) which is a transverse wave. Using Helmholtz's decomposition, we represent the displacement field vector  $\mathbf{u}$  as

$$\mathbf{u} = \nabla \phi + \nabla \times \boldsymbol{\psi}, \quad (3.2)$$

where  $\phi$  the scalar potential and  $\boldsymbol{\psi}$  are the vector potential. Each term of 3.2 show the divergent and the rotation component of  $\mathbf{u}$  respectively. Substitute Eq. 3.2 into Eq. 3.1 and after some vector algebra, one can obtain two wave equations;

$$\ddot{\phi} = v_L^2 \nabla^2 \phi, \quad (3.3)$$

$$\ddot{\boldsymbol{\psi}} = v_T^2 \nabla^2 \boldsymbol{\psi}, \quad (3.4)$$

where  $v_L, v_T$  are defined as

$$v_L = \sqrt{\frac{\lambda + 2\mu}{\rho}}, \quad v_T = \sqrt{\frac{\mu}{\rho}}. \quad (3.5)$$

These phase velocities;  $v_L, v_T$  represent that of the P-wave and the S-wave. Show this relationships. Because the scalar potential and the vector potential are obey the wave equation Eq.3.3 and Eq.3.4 respectively, the general solutions of these potentials are given as

$$\phi = \phi_0(\omega t - \mathbf{k} \cdot \mathbf{x}) \quad (3.6)$$

$$\boldsymbol{\psi} = \boldsymbol{\psi}_0(\omega t - \mathbf{k} \cdot \mathbf{x}), \quad (3.7)$$

where  $\omega, \mathbf{k}$  are the angular frequency and the wave vector. One can obtain the divergent component of displacement field vector  $\mathbf{u}$  as

$$\mathbf{u}_{\text{div}} = \nabla \phi_0(\omega t - \mathbf{k} \cdot \mathbf{x}) = -\mathbf{k} \phi. \quad (3.8)$$

The displacement of this wave  $\mathbf{u}_{\text{div}}$  whose phase velocity is  $v_L$  propagates along with direction of the wave vector. Therefore  $v_L$  is the phase velocity of a longitudinal wave called P-wave. On the other hands, one can obtain the rotation component of  $\mathbf{u}$  as

$$\mathbf{u}_{\text{rot}} = \nabla \times \boldsymbol{\psi}_0(\omega t - \mathbf{k} \cdot \mathbf{x}) = -\mathbf{k} \times \boldsymbol{\psi}. \quad (3.9)$$

This displacement vector  $\mathbf{u}_{\text{rot}}$  whose phase velocity is  $v_T$  is perpendicular to the wave vector. Therefore,  $v_T$  is the phase velocity of a transverse wave called S-wave. Furthermore, because  $\lambda$  and  $\mu$  are positive numbers,

$$v_L > v_T. \quad (3.10)$$

Therefore, the longitudinal wave is faster than the transverse wave.

### Rayleigh waves

Rayleigh wave は P 波と S 波の干渉によって生じる []。ここでは Z 軸を鉛直方向とした直交直線座標系の x-z 面内で振動する弾性波を考える。z=0 を自由表面とし、x 軸に沿って P 波と S 波が同じ速度  $v_R = \omega/k$  ( $\omega$  is angular frequency and  $k$

is the wave vector) で伝搬する場合を考えると、ポテンシャル  $\phi$  と  $\psi$  は、それぞれ以下のように表すことができる。

$$\phi = F(z) \exp[i(kx - \omega t)], \quad (3.11)$$

$$\psi = G(z) \exp[i(kx - \omega t)] \quad (3.12)$$

Eq.3.11 と Eq.3.11 を波動方程式 Eq.3.3, Eq.3.4 に代入すれば、レイリー波の特性方程式が導かれる;

$$\left(\frac{c_R^2}{c_S^2}\right)^3 - 8\left(\frac{c_R^2}{c_S^2}\right)^2 + 8\left(3 - \frac{2}{\gamma^2}\right)\left(\frac{c_R^2}{c_S^2}\right) - 16\left(1 - \frac{1}{\gamma^2}\right) = 0 \quad (3.13)$$

where  $\gamma \equiv v_L/v_T$ . In case that  $0 < (c_R^2/c_S^2) < 1$ , the velocity has physically meaningful value. According to Eq.3.13, the ratio  $c_R/c_S$  is a function of the ratio of  $\gamma$ . たとえば、KAGRA と同じ山の下に建設された 100m の重力波望遠鏡 CLIO での P 波と S 波の位相速度はそれぞれ AA、BB である [7] ので、 $\gamma = 1.82$  である。したがってこのときのレイリー波の位相速度は CC である。

### 3.1.2 Reduction Effect in the Deep Sites

レイリー波の振幅は深さに依存しており、深いほど小さくなる。

### 3.1.3 Reduction Effect of the Short Baseline

For interferometric gravitational-wave detectors which need a precise length control of the optical resonate cavity, it is appropriate to consider about the relative displacement between two points rather than the displacement of single point. In this subsection, the reduction effect of relative displacement if the seismic noise at each point have a correlation is discribed.

#### Differential Motion and Common Motion

Motions of the two points can be represented as the differential motion and the common motion. Displacement of both differential motion and common motion of the two points shown in Figure(??) are defined as

$$u_{\text{diff}} \equiv \frac{u_1 - u_2}{\sqrt{2}}, u_{\text{comm}} \equiv \frac{u_1 + u_2}{\sqrt{2}} \quad (3.14)$$

where  $u_1(x, t)$  and  $u_2(x, t)$  are the displacement of each points. These two motions defined in Eq.(3.14) are normalized by  $\sqrt{2}$  due to conserve the total power.

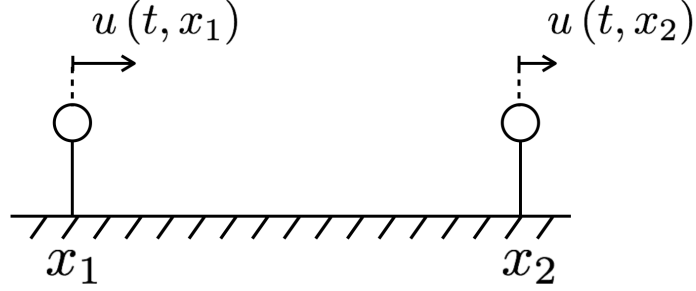


**Figure 3.1:** The displacements of the two points which are separated  $L$  in  $X$  axis.

### Common and Differential Motion Ratio (CDMR)

CDMR is defined as the powers of common motion over the differential motion as bellow,

$$\text{CDMR} \equiv \sqrt{\frac{\text{Common Motion}}{\text{Differential Motion}}} = \sqrt{\frac{P_{\text{comm}}(\omega)}{P_{\text{diff}}(\omega)}} \quad (3.15)$$

where  $P_{\text{comm}}, P_{\text{diff}}$  are the power spectral densities (PSDs) of the differential motion and common motion, respectively. Each PSDs are converted from the autocorrelation function of these by the Wiener-Khinchin theorem.

First, autocorrelation function  $C_{\text{diff}}$  of the differential motion is given by its definition in Eq.(3.14)

$$C_{\text{diff}}(\tau) = \frac{1}{2} \left\langle \left[ x_1(t) - x_2(t) \right] \left[ x_1(t + \tau) - x_2(t + \tau) \right] \right\rangle \quad (3.16)$$

$$= \frac{1}{2} \left[ C_{11}(\tau) - C_{12}(\tau) - C_{21}(\tau) + C_{22}(\tau) \right], \quad (3.17)$$

,where  $C_{ij}$  are the autocorrelation functions of each point and defined as  $C_{ij} \equiv \langle x_i(t)x_j(t + \tau) \rangle$ , ( $i = 1, 2, j = 1, 2$ ). Therefore, the power spectrum density of differential motion  $P_{\text{diff}}(\omega)$  can be computed as

$$P_{\text{diff}}(\omega) = \frac{1}{2} \left[ P_1(\omega) + P_2(\omega) - P_{12}(\omega) - P_{12}^*(\omega) \right] \quad (3.18)$$

$$= \frac{1}{2} \left[ P_1 + P_2 - \text{Re} [\gamma] \times 2\sqrt{P_1 P_2} \right] \quad (3.19)$$

where  $P_1(\omega), P_2(\omega)$  are the power spectrum densities of each points, and  $P_{12}(\omega)$  are the cross spectrum between two point. The parameter  $\gamma$  is the complex coherence between them defined below,

$$\gamma \equiv \frac{P_{12}}{\sqrt{P_1 P_2}}. \quad (3.20)$$



Here, assuming that seismic wave propagating each points does not decay, which means  $P_1 = P_2 \equiv P$ , one can compute the  $P_{\text{diff}}(\omega)$  as

$$P_{\text{diff}}(\omega) = P(1 - \text{Re}[\gamma]). \quad (3.21)$$

Therefore, the PSDs of the common motion can be calculated as

$$P_{\text{comm}}(\omega) = P(1 + \text{Re}[\gamma]). \quad (3.22)$$

Finally, CDMR defined Eq.(3.15) in case the seismic wave does not decay is represented as

$$\text{CDMR} = \sqrt{\frac{1 + \text{Re}[\gamma]}{1 - \text{Re}[\gamma]}}. \quad (3.23)$$

Eq.(3.23) indicate that CDMR can be expressed by only the coherence  $\gamma$  between of two points. For example, CDMR tends to be larger when  $\gamma$  close to 1. This means that the differential motion is more less than the common motion because the two points move together in the same direction.

## 3.2 Seismic Noise

Characteristics of seismic noise are related with its origin spatially and temporally. The noise sources are spreaded anywhere; foot steps, traffics and ocean waves, and these amplitude depends on day-night or weather condition.

As summarized in Table 3.1, the seismic noises above 1 Hz are clearly correlated with cultural activities, and that below this frequency are excited by the natural phenomena [8]. This boundary frequency between cultural or natural, 1 Hz, is depends on the soil structure. At the sediment site such as the LIGO[9] and Virgo site[10], the former noise can be shifted to a lower frequency and appear below 1 Hz. On the other hands, at the hard rock site such as KAGRA site, the cultural noise can be distinguished from the natural noise for its diurnal variability and apparent only above 1 Hz.

**Table 3.1:** Two types of seismic noise

Type of noise	Frequency Band	Sources
Cultural Noise	> 1 Hz	wind, traffic, machinaries, foot steps
Natural Noise	< 1 Hz	ocean, air pressure, earth tides

### 3.2.1 Cultural Noises

The cultural seismic noise contaminates the sensitivity of gravitational-wave detectors in the frequency range of interest for gravitational-waves sources, above

1 Hz. In this frequency band, the cultural noise is dominated by winds or human activities. For example, seismic noise from traffic near the detectors is reported at LIGO site [11], and noise from the vibrations of building excited by winds is reported at Virgo site [12].

### 3.2.2 Natural Noises

The natural seismic noise affects the stability of the GW detectors below 1 Hz because it deforms largely the bedrock on which mounted the detectors. これら natural seismic noise は低周波になればなるほどグローバルな励起源によるノイズを反映しており、パワースペクトル密度は大きくなる。

#### Microseisms

Microseisms which power spectrum has peaks in 50–200 mHz are excited by oceanic waves. These seismic waves can be categorized by the generating mechanism of these [13]. First, the primary ocean microseisms are generated only in shallow waters in coastal regions. In this regions, the water wave energy can be converted directly into seismic energy either through vertical water pressure variations, or by the impacts of surf on the shores. There are correlation between this microseismic peak and the swell at the beaches was known starting from the data sets studied by [14]. Second, the secondary ocean microseisms could be explained by the superposition of ocean waves of equal period traveling in opposite directions. Therefore, generating standing gravity waves of half the period [15].

The RMS amplitude spectral of both type of the microseisms are strongly depends on the low pressure on the ocean [16].

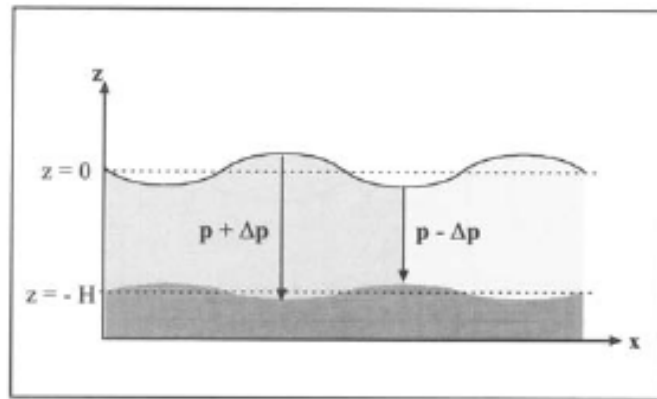
#### Deformation of the bedrock

In few mHz, ground deformed by the air pressure changes. ...  
...

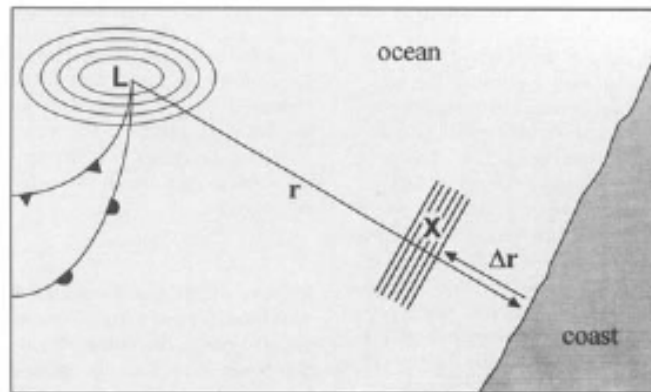
Below more lower frequency, the earth deformed by tidal forces due to the attraction of the Sun and the Moon.

### 3.2.3 Spatial Seismic Noise Changes

地面振動は場所や時間により異なる。Peterson らは、世界の 75 箇所の基地にある地震計の数年分のデータから地面振動のノイズスペクトルを得た。これらデータは地表と地下両方のデータを含み、並進成分と垂直成分を含む。NHNM は、内陸の沖積層で地面が揺れやすい場所や、沿岸地域で脈動や人間の活動の影響を受けやすい場所の地面振動を反映している。一方で NHNM は、とくに 0.1Hz 以下では、広範囲の複数の地震計の垂直成分で得られた地面振動のノイズフロアである。



(a) Generating mechanism of the primary microseisms.  
引用先の図をコピーしているの、自分で描いたのに差し替える。



(b) Generating mechanism of the secondary microseisms. 引用先の図をコピーしているの、自分で描いたのに差し替える

**Figure 3.2:** Generating mechanism of the microseisms. (a) describes the mechanism of the primary microseisms. (b) describes the mechanism of the secondary microseisms.

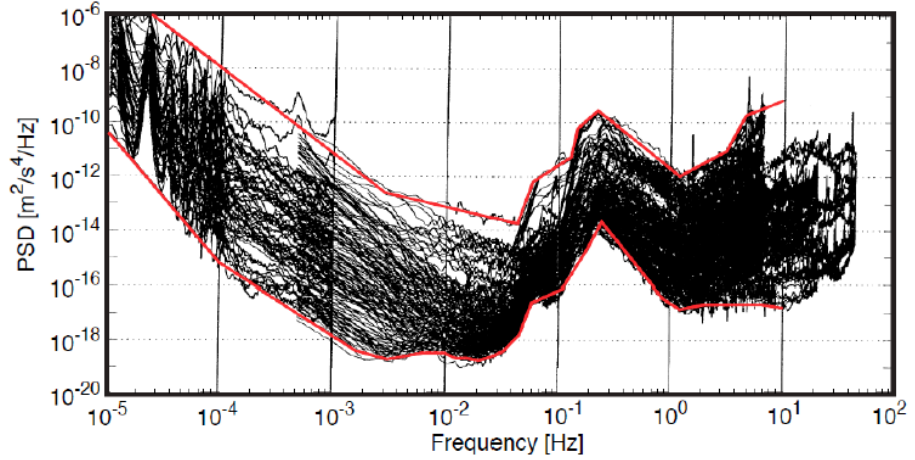


**Figure 3.3:** PSD of the seismic noise obtained by Peterson in several place in the world[17] (この図は自分で書き直す必要あり。)

### 3.3 Study of Temporal Seismic Noise at KA-GRA

#### 3.3.1 Overview

本節では、KAGRA での地面振動の大きさが時間帯や季節の違いでどのように変化するか調べた。基本的に地震などの突発現象を除けば、地面振動は定常的な振る舞いを示すが、その RMS 振幅は時間依存である。例えば、人間由来の地面振動は夜間になると静かで、波浪由来の脈動は天気が悪化するとうるさくなる。また日本の場合、初秋は台風によって、冬は日本海低気圧によって脈動がうるさくなることが知られている []。とくに後者の脈動がうるさいと、干渉計の稼働が妨げられ、DutyCycle を低下してしまう。このような理由から、地面振動の時間依存性を知ることが、干渉計の稼働の安定性を議論するうえで重要である。

地面振動の振幅スペクトルの分布は、およそ 1 年間の地震計の時系列データからもとめた。このデータには、地震計のメンテナンスによるデータの欠損や、地震などの突発的な地面振動のデータが含まれている。そのため、スペクトルを計算するためにこれらデータを取り除き、およそ 1 時間 (4096 秒) 区切りのデータ・セットを用意した。これらデータ・セットごとに振幅スペクトルを計算し、分布をもとめた。

#### 3.3.2 Experimental Arrangement

Seismic motion is measured by a seismometer installed on the second floor of the X-end area. This area is placed 200 m underground from the surface of the mountain. Comparison to corner area, human activity in the end area is

less because the corner area has parking lots. Comparison to the Y-end area, there is no entrance connected to other mines. Therefore, the X-end area is relatively quiet in the KAGRA mine, regarding the seismic noise induced by human activity.

In this study, Trillium 120-QA which is known as three-component, very broadband, and low-noise seismometer, was used. These three outputs are proportional to the ground velocity of two horizontal and one vertical, respectively. The feature of the low-noise can resolve Peterson's new low-noise model (NLNM) and new high-noise model (NHNM) [17].



**Figure 3.4:** Trillium 120-QA installed on the second floor at X-end area, which is covered by black thermal insulation cover

As shown in fig 3.4, the seismometer is housed in the black thermal insulation cover according to the installation manual [18]. Thermal insulation protects two broad categories of thermal couplings that can cause unwanted noise [18]. First is the direct coupling to the sensitivity. This coupling typically increases the noise of the vertical channel as a periodic diurnal variation caused by the day-to-night temperature cycle, because the springs that suspended the inertial masses are temperature sensitive. The second is the coupling to tilt from the thermal fluctuation. Tilt converts the vertical acceleration of gravity into horizontal acceleration. This thermally induced tilt noise on the horizontal will be larger than the direct thermal coupling on the vertical channel. To be low sensitivity to both tilt and temperature, this model has a function to center the inertial mass after the initial installation.

The signals of the seismometer is recorded through the data acquisition system developed by LIGO [19]. The analog signal is converted to digital signal by the 16 bit analog-to-digital converters (ADC) with 16384 Hz sampling. This analog signal is amplified with 30 db so that the ADC noise does not mask this signal.

### 3.3.3 Data Selection

およそ 1 年分の地震計のデータをつかった。スペクトルの計算のために、一年分のデータを 4096 秒のセグメントに分割し、その中からデータの欠損などの異常値を取り除いた。解析に使ったセグメントを Fig?? に示す。14-15 週と 33-34 週に生じた大きなデータの欠損期間を除いて、一年を通してデータが取得できている。セグメントは XX 個あり、全体の XX% を占める。

### 3.3.4 Data Processing

振幅スペクトルの推定は 50% オーバーラップした 32 個のセグメントの平均で得た。それぞれのセグメントの FFT の計算は、まず dtrend をして線形成分を取り除き、Hanning 窓にかけてから行った。32 回の平均をおこなったスペクトルは自由度 32 のカイ二乗分布に従う。自由度  $\nu$  のときの  $100(1 - \alpha)\%$  の信頼区間は、周波数  $f$  でのスペクトルの推定量を  $\hat{G}(f)$  とすると、

$$\frac{\nu \hat{G}(f)}{\chi^2(\nu, 1 - \frac{\alpha}{2})} \leq G(f) \leq \frac{\nu \hat{G}(f)}{\chi^2(\nu, \frac{\alpha}{2})} \quad (3.24)$$

で与えられる。したがって、95% の信頼区間は

$$\nu / \chi^2(\nu, 1 - \frac{\alpha}{2}) \leq G(f) / \hat{G}(f) \leq \nu / \chi^2(\nu, \frac{\alpha}{2}) \quad (3.25)$$

となり、自由度 32 の場合、推定量の 0.65 から 1.75 の範囲になる。

### 3.3.5 Results

すべてのセグメントから求めた振幅スペクトル密度を振幅に換算したものを Fig. ?? に示す。赤の実線は垂直成分の 50 パーセンタイルで、下と上に 10 と 90 パーセンタイルを示す。青の実線は X 軸と Y 軸の二乗和から求めた並進成分であり、同様に 10, 50, 90 パーセンタイルを示す。緑点線は Trillium120 のデータシートから引用した Selfnoise である。黒の点線は Peterson の NLNM と NHNM である。

測定で得られた地面振動は、40mHz 以上では並進成分も垂直成分も同じ振幅スペクトル密度をもつ。40mHz 以下で並進成分が垂直成分よりも大きい、これは付録で後述しているとおり、無相関なノイズである。おそらく温度ゆらぎから生じる傾斜カップリングだと考えられる。

Peterson のスペクトルと測定で得た 10 パーセンタイルを比較すると、0.1 から 2Hz をのぞいて、NLNM と同じである。0.1Hz 以下では垂直成分は地面振動のノイズレベルと同等であり、2Hz 以上は、並進も垂直成分も、地下環境のおかげで静かである。

対照的に 0.1 から 2Hz の帯域では、並進成分も垂直成分も NLNM より数倍大きい。これは KAGRA が富山湾から 40km の距離にあり、比較的脈動の影響を受けやすいためと考えられる。

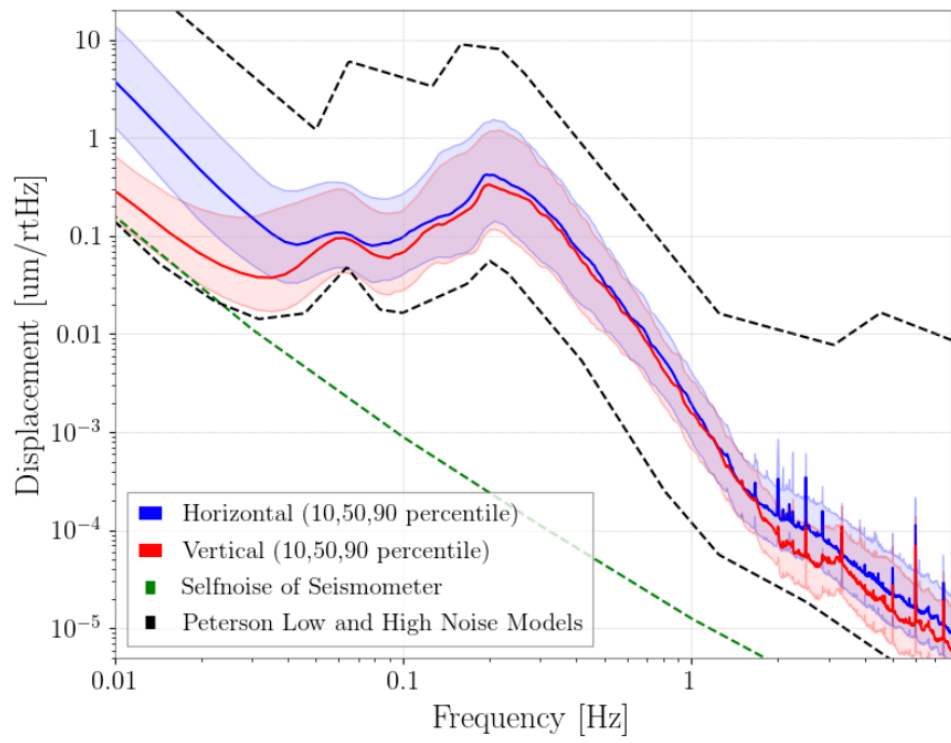


Figure 3.5

## 3.4 Study of Differential Motion Reduction

### 3.4.1 Introduction

The motion of two mirrors in the cavity have two modes. One is differential motion, which is the length change of that. Another one is common motion, which is the motion of the center of the cavity. In terms of the length control, it is important that the RMS amplitude of differential motion is as small as possible. Actually, the amplitude of these two motions are the same each other when the mirrors moves with no coherence. However, when a coherence exists, the common motion tends to be larger than the differential one.

As discussed in this section, the coherence depends on both, the arm length and the wavelength of seismic waves. For example, if the arm length is much more smaller than the wavelength, the mirrors move together. This means that the common motion is greater than the differential motion.

The ratio of the amplitudes of the differential motion over common motion is newly defined as Common and Differential Motion Ratio (CDMR). It is useful to know how the ground reduces the differential motion or increase the common motion.

### 3.4.2 Overview

Fig.3.6 に示すように





**Figure 3.6:** Seismometers for measurement of the differential motion reduction

#### **3.4.3 Reduction in X-arm Scale**

#### **3.4.4 Reduction in Other Short Scale**

### **3.5 Summary of the Chapter**



**Figure 3.7:** ...



**Figure 3.8:** ...

## Chapter 4

# Geophysics Interferometer (GIF)

### 4.1 Overview

#### 4.1.1 Laser Strainmeter for Geophysics

#### 4.1.2 Motivation in GW detectors

### 4.2 Working Principle

#### 4.2.1 Asymmetric Michelson Interferometer

$$\phi = 2\pi \frac{2(l_x - l_y)}{\lambda} \sim 4\pi \frac{l_x}{\lambda} \quad (4.1)$$

$$|d\phi| = 4\pi \frac{l_x}{\lambda} \left( \left| \frac{d\lambda}{\lambda} \right| + \left| \frac{dl_x}{l_x} \right| \right) \quad (4.2)$$

#### 4.2.2 Response to the seismic strain

The response of the strainmeter to seismic waves have characteristics of the low pass filter. To calculate this response, it is assumed that the plane seismic waves which displacement  $u(x, t)$  is represented as  $u(x, t) = u_0 e^{i(\omega t - kx)}$  with angular frequency of  $\omega$  and wave number of  $k$ , propagate along with the direction of the base-line of the strainmeter. The length fluctuation between two mirrors separated with  $L$  can be expressed as

$$\Delta L(t) \equiv u(0, t) - u(L, t) \quad (4.3)$$

$$= u(0, t) - u(0, t - \tau), \quad (4.4)$$

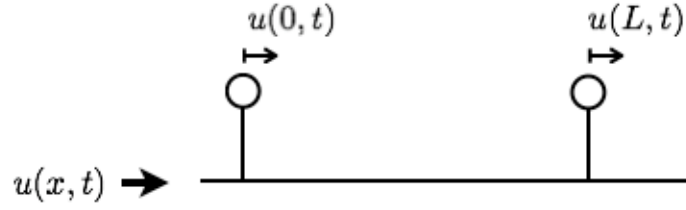


**Figure 4.1:** The displacements of the two points which are separated  $L$  in  $X$  axis.

where  $\tau = L/v$  is the time delay. The transfer function from the displacement to the length fluctuation is

$$H_{\text{disp}}(s) \equiv \frac{\Delta L(s)}{u(s)} = 1 - \exp(-\tau s) \quad (4.5)$$

Because the strain amplitude  $\epsilon(x, t)$  is defined as  $\epsilon(x, t) \equiv \frac{du}{dx}$ , the strain

$$\epsilon(x, t) \equiv \frac{du}{dx} = \frac{du}{dt} \frac{dt}{dx} \quad (4.6)$$

$$= u(x, t)' \frac{1}{v} \quad (4.7)$$

Therefore, the response of the strainmeter to the seismic strain is given

$$H_{\text{strain}}(s) \equiv \frac{\Delta L(s)}{\epsilon(s)} = \frac{\Delta L(s)}{\frac{s}{v}u(s)} = (1 - \exp(-\tau s)) \frac{v}{s} \quad (4.8)$$

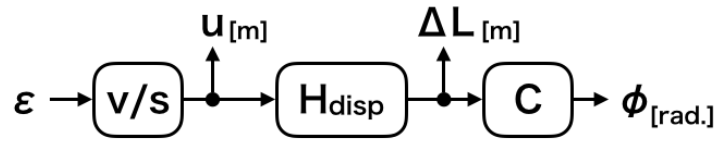


**Figure 4.2**

### 4.2.3 Signal Detection Scheme

#### Quadrature Phase Detection

### 4.2.4 Noise

どういふノイズが原理的に存在するか述べる。空気ゆらぎ、周波数雑音を述べる。

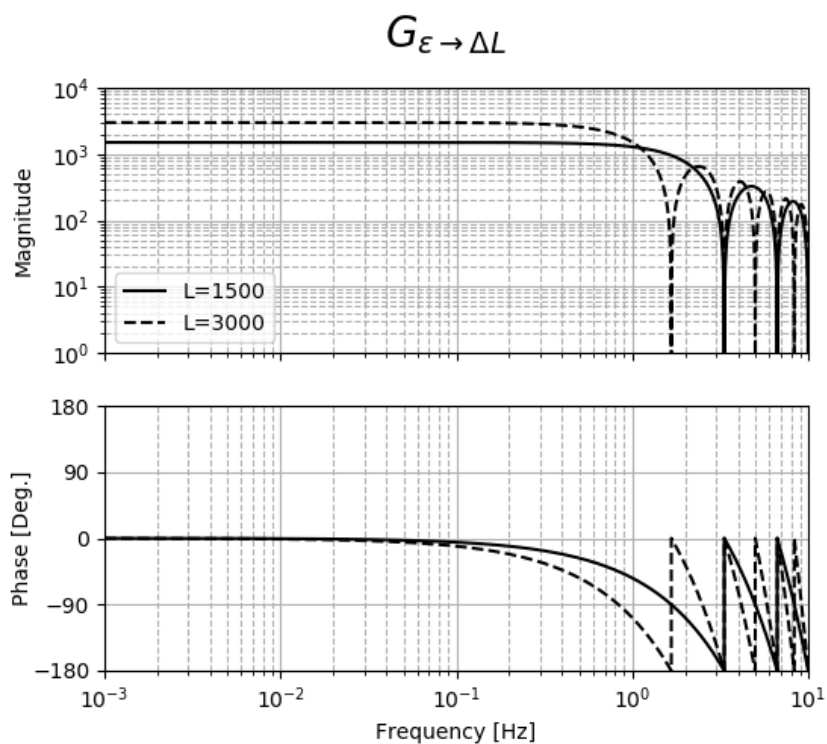


Figure 4.3

## 4.3 Optics Design

...

### 4.3.1 Overview

Optical layout is shown in Fig. 4.4. Optics of GIF is categorized by three category; mode-matching optics, core optics and frequency stabilized laser.

### 4.3.2 Design Concept

設計で考慮しなければならない点は\*干渉位置で2つのモードが合っていること  
\*できるだけ光学系は小さくすることである。

腕の長さから生じるモードのズレを小さくするために、エンドリフレクタでビームウエストを持つようにする。



Figure 4.4

#### 4.3.3 Input Output Optics

#### 4.3.4 Core Optics

#### 4.3.5 Frequency Stabilized Laser

### 4.4 Data Aquisition System

#### 4.4.1 Realtime Processing

#### 4.4.2 ...

### 4.5 Summary of the Chapter

本章で述べたパラメータを表にまとめる。

## Chapter 5

# Arm Length Compensation System for Global Seismic Control

### 5.1 Introduction

Seismic noise cause two main problems to the terrestrial gravitational-wave detectors. First one is the limitation of the sensitivity. Amplitude spectrum density of the seismic noise, is empirically known as

$$\sim \frac{10^{-7}}{f^2} \text{ m}/\sqrt{\text{Hz}}, \quad (5.1)$$

where  $f$  is a frequency of the spectrum. This noise limits the sensitivity of the detectors in lower frequency typically below 10 Hz even after the attenuation by the vibration isolation systems. On the other hands, second problem is the decrease of the duty cycle of the GW detectors. Laser interferometric detector has an Fabry-Perot optical resonant cavities to enhance the sensitivity of GWs. This optical cavity only resonant within the narrow linewidth of few nm, whereas the seismic noise is larger than this width by two orders of magnitudes.

Underground can resolve these problems. Underground is more quiet than the surface of the ground [20]. Especially, the underground seismic noise above 1 Hz is effectively reduced than the noise on surface of the ground [21]. For example, a laser interferometer gravitational wave antenna with a baseline length of 20 m (LISM) constructed underground have demonstrated the stable performance of the detector by resulting the high duty cycle of 99.8 % [22].

しかし、KAGRA のような 3km の長期線のレーザー干渉計では、LISM のように安定して可動させることは難しいとされている。なぜならば、地面振動による基線長変動は、基線長が長いほどその影響は大きいためである。後述する §3.3 に

よれば、0.2Hz の脈動による基線長変動への影響は、KAGRA は LISM の 150 倍ある一方で、表 5.1 に示すように、線幅はおよそ 17 倍しかない。つまり KAGRA は LISM と比べて、線幅に対して地面振動による基線長伸縮はおよそ 1 桁大きいことを意味する。このような長期線化による問題は、KAGRA などの第二世代の検出器だけの問題ではなく、ET などの数 10km の基線長を計画する第 3 世代の検出器にとって同様の問題となる。

**Table 5.1:** Comparison of the line width of the arm cavity

	Finess	Line width [ $\mu\text{m}$ ]	Baseline length [m]
LISM	25000	0.021	20
KAGRA	1500	0.35	3000



## 5.2 Basics in Vibration Isolation and Control Technique

### 5.2.1 Passive Vibration Isolation

Single Pendulum

Multi Pendulum

### 5.2.2 Active Vibration Isolation

### 5.2.3 Sensor Belnding Control Technique

### 5.2.4 2 Types Feedforward Control Techniques

Feedforward at Feedback Point

Feedforward at Error Point

### 5.2.5 Toward the Global Seismic Control

Overview

Suspension Point Interferometer

## 5.3 Difficulties in the Global Seismic Control

### 5.3.1 Overview

### 5.3.2 Actuator Range Limit

### 5.3.3 ...

### 5.3.4 ...

## 5.4 Arm Length Compensation Using Geophysics Interferometer

### 5.4.1 Concept

### 5.4.2 Geophysics Interferometer for Sensing the Arm Length

### 5.4.3 Arm Length Compensation

### 5.4.4 Requirements

## 5.5 Summary of the Chapter



## Chapter 6

# Demonstration of Arm Length Compensation Control

### 6.1 Experimental Arrangement

#### 6.1.1 ...

### 6.2 Results

#### 6.2.1 ...

### 6.3 Discussion and Summary of the Chapter

#### 6.3.1 Discussion

#### 6.3.2 Summary



## Chapter 7

# Conculusion and Future Directions

### 7.1 Conclusion

### 7.2 Future Directions



## Appendix A

# Theory of Seismic Waves

### A.1 Rayleigh 波

(レイリー波の導出。)

### A.2 Depth Dependence

(レイリー波の振幅が深さに依存していることを述べる。)





# Bibliography

- [1] T Uchiyama, K Furuta, M Ohashi, S Miyoki, O Miyakawa, and Y Saito. Excavation of an underground site for a km-scale laser interferometric gravitational-wave detector. *Classical and Quantum Gravity*, 31(22):224005, 2014. [Link](#).
- [2] Yukio Isozaki, Kazumasa Aoki, Takaaki Nakama, and Shuichi Yanai. New insight into a subduction-related orogen: a reappraisal of the geotectonic framework and evolution of the japanese islands. *Gondwana Research*, 18(1):82–105, 2010. [Link](#).
- [3] T Akutsu and et. al. Construction of kagra: an underground gravitational-wave observatory. *Progress of Theoretical and Experimental Physics*, 2018(1), 01 2018. [Link](#).
- [4] Yoichi Aso, Yuta Michimura, Kentaro Somiya, Masaki Ando, Osamu Miyakawa, Takanori Sekiguchi, Daisuke Tatsumi, and Hiroaki Yamamoto. Interferometer design of the kagra gravitational wave detector. *PHYSICAL REVIEW D Phys Rev D*, 88:043007, 2013. [Link](#).
- [5] Kentaro Somiya. Detector configuration of kagra the japanese cryogenic gravitational-wave detector. *Classical and Quantum Gravity*, 29(12):124007, jun 2012. [Link](#).
- [6] Okutomi Koki. *Development of 13.5-meter-tall Vibration Isolation System for the Main Mirrors in KAGRA*. PhD thesis, SOKENDAI, The Graduate University for Advanced Studies, 2019. [Link](#).
- [7] 竹本修三, 新谷昌人, 赤松純平, 森井互, 東敏博, 福田洋一, 尾上謙介, 市川信夫, 川崎一朗, 大橋正健, et al. 神岡鉱山における 100 メートルレーザー伸縮計について. 2003.
- [8] Sylvette Bonnefoy-Claudet, Fabrice Cotton, and Pierre-Yves Bard. The nature of noise wavefield and its applications for site effects studies: A literature review. *Earth-Science Reviews*, 79(3-4):205–227, 2006.
- [9]

- [10] M G Beker, J F J van den Brand, E Hennes, and D S Rabeling. Newtonian noise and ambient ground motion for gravitational wave detectors. *Journal of Physics: Conference Series*, 363:012004, jun 2012.
- [11] R. Schofield et al. Source and propagation of the predominant 1-50 hz seismic signal from off-site at ligo-hanford. In LIGO Scientific Collaboration Meeting, Hanford, August 2000.
- [12] F Acernese, P Amico, N Arnaud, D Babusci, R Barillé, F Barone, L Barsotti, M Barsuglia, F Beauville, MA Bizouard, et al. Properties of seismic noise at the virgo site. *Classical and Quantum Gravity*, 21(5):S433, 2004.
- [13] P Bormann. New manual of seismological observatory practice. *GFZ German Research Centre for Geosciences*, 2012. [Link](#).
- [14] RA Haubrich, WH Munk, and FE Snodgrass. Comparative spectra of microseisms and swell. *Bulletin of the Seismological Society of America*, 53(1):27–37, 1963. [Link](#).
- [15] Michael Selwyn Longuet-Higgins. A theory of the origin of microseisms. *Philosophical Transactions of the Royal Society of London. Series A, Mathematical and Physical Sciences*, 243(857):1–35, 1950. [Link](#).
- [16] L Naticchioni, M Perciballi, F Ricci, E Coccia, V Malvezzi, F Acernese, F Barone, G Giordano, R Romano, M Punturo, R De Rosa, P Calia, and G Loddo. Microseismic studies of an underground site for a new interferometric gravitational wave detector. *Classical and Quantum Gravity*, 31(10):105016, may 2014.
- [17] Jon R Peterson. Observations and modeling of seismic background noise. Technical report, US Geological Survey, 1993.
- [18] Nanometrics Inc., 250 Herzberg Road Kanata, Ontario, Canada K2K 2A1. *Trillium 120Q/QA User Guide*, 04 2017.
- [19] Rolf Bork, R Abbott, D Barker, and J Heefner. An overview of the ligo control and data acquisition system. *arXiv preprint physics/0111077*, 2001.
- [20] Jerry A Carter, Noel Barstow, Paul W Pomeroy, Eric P Chael, and Patrick J Leahy. High-frequency seismic noise as a function of depth. *Bulletin of the Seismological Society of America*, 81(4):1101–1114, 1991.
- [21] LCGT collaboration. Lcgt design document version 3.0. Technical Report JGW-T0400030-v4, Institute for Cosmic Ray Research, University of Tokyo, JGW document, 11 2009.

- [22] Shuichi Sato, Shinji Miyoki, Souichi Telada, Daisuke Tatsumi, Akito Araya, Masatake Ohashi, Yoji Totsuka, Mitsuhiro Fukushima, Masa-Katsu Fujimoto, LISM Collaboration, et al. Ultrastable performance of an underground-based laser interferometer observatory for gravitational waves. *Physical Review D*, 69(10):102005, 2004.